# MIMO Channel Measurements at 300 MHz for an elevated and a peer-to-peer scenario

PETER HOLM, GUNNAR ERIKSSON,
AND KIA WIKLUNDH


FOI, Swedish Defence Research Agency, is a mainly assignment-funded agency under the Ministry of Defence. The core activities are research, method and technology development, as well as studies conducted in the interests of Swedish defence and the safety and security of society. The organisation employs approximately 1000 personnel of whom about 800 are scientists. This makes FOI Sweden's largest research institute. FOI gives its customers access to leading-edge expertise in a large number of fields such as security policy studies, defence and security related analyses, the assessment of various types of threat, systems for control and management of crises, protection against and management of hazardous substances, IT security and the potential offered by new sensors.

FOI
Swedish Defence Research Agency
Command and Control Systems
P.O.Box 1165
SE- 581 11 LINKÖPING

Phone: +46 13 37 80 00
Fax: +46 13 37 81 00

www.foi.se

FOI-R--3282--SE
ISSN 1650-1942

Scientific Report
November 2011

**Command and Control Systems**

Peter Holm, Gunnar Eriksson, and Kia Wiklundh

# MIMO Channel Measurements at 300 MHz for an elevated and a peer-to-peer scenario

| | |
|---|---|
| Title | MIMO Channel Measurements at 300 MHz for an elevated and a peer-to-peer scenario |
| Titel | MIMO-kanalen i stadsmiljö vid 300 MHz för ett eleverat och ett peer-to-peer scenario |
| Report No. / Rapportnr | FOI-R--3282--SE |
| Report Type | Scientific Report |
| Rapporttyp | Vetenskaplig rapport |
| Month / Månad | November / November |
| Year / Utgivningsår | 2011 |
| Pages / Antal sidor | 44 |
| ISSN | 1650-1942 |
| Customer / Kund | FM |
| Project No. / Projektnr | E53053 |
| Approved by / Godkänd av | Anders Törne |



FOI, Swedish Defence Research Agency
Command and Control Systems
P.O. Box 1165
SE-581 11 LINKÖPING

FOI, Totalförsvarets Forskningsinstitut
Avdelningen för Ledningssystem
Box 1165
581 11 LINKÖPING

## Abstract

Multiple-input multiple-output (MIMO) systems operating at frequencies in the upper VHF and lower UHF region are attractive for communication applications where robustness is of high importance, e.g. in military tactical networks and emergency response systems. When designing and evaluating such systems, knowledge of realistic wave propagation conditions is required. This report presents results from an urban MIMO measurement campaign at 300 MHz performed in Malmö, Sweden. The measurement scenarios consist of both a peer-to-peer scenario and an elevated scenario. Measurements are performed along 23 receiver routes and for two fixed transmitter locations, using antenna arrays mounted on two cars. Channel characteristics and ergodic capacity for the $7 \times 7$ MIMO channels are extracted from the measured data. A path-gain model is derived for the measured scenario, and the distributions of the large-scale fading, the Ricean $K$-factor, the delay spread, and the ergodic capacity are studied in detail. The correlation distance of the different channel parameters is also examined. Furthermore, the analysis reveals that several of the channel parameters are correlated, and also have a strong correlation with the capacity.

Keywords: MIMO, channel, measurement, radio, VHF, UHF, wave propagation

## Sammanfattning

För robusta trådlösa kommunikationslösningar är flerantennsystem, s.k. MIMO-system, som arbetar på frekvenser i VHF- och UHF-bandet en intressant lösning; till exempel för system för taktisk kommunikation eller kommunikation för civil säkerhet. Vid design och utveckling av sådana system är det viktigt med kännedom om radiokanalens egenskaper i relevanta miljöer. I rapporten presenteras resultat från en MIMO-mätkampanj genomförd vid 300 MHz i stadsmiljö i Malmö. Mätkampagen innefattar både ett peer-to-peer-scenario respektive ett eleverat scenario. Mätningar genomfördes mellan två fasta sändarplatser och 23 mottagarsträckor. Sändaren och mottagaren var placerade i varsin bil med MIMO-mätantennen monterad på taket. Kanalkaraktäristik och kapacitet utvanns ur de uppmätta $7 \times 7$ MIMO-kanalerna. Från mätscenariot tas en modell av transmissionsförlusten fram och fördelningarna för den storskaliga fädningen, $K$-faktorn, tidsspridningen och kapaciteten studeras. För de olika parametrarna undersöks även korrelationsavståndet. Analyserna visar att flera av kanalparametrarna är korrelerade och även har en stark korrelation med kapaciteten.

Nyckelord: MIMO, kanalmätning, kanal, mätning, radio, VHF, UHF, vågutbredning

# Contents

# 1 Introduction

The Swedish Armed Forces is undergoing a process of change in which a mission-based force is developed and ready to be deployed anywhere conflicts arise. For mission success it is essential to achieve battlefield awareness and information superiority. Since, communication is an essential part to accomplish this, special effort should be taken to develop mobile networks that are robust reliable and with high capacity. The services needed in a mobile tactical wireless network to achieve battlefield awareness and information superiority have high demands on communication capacity. This must also be achieved in a variety of environments, including urban areas. Peer-to-peer communications are important for such networks, as well as for many other applications, e.g. emergency response systems. From a wave propagation point of view, the peer-to-peer communication scenario is more challenging than scenarios with elevated base stations, e.g. cellular communication systems. Due to the low height of both the transmitter (Tx) and receiver (Rx), line-of-sight (LOS) conditions rarely exists. The robustness of wireless communication systems is strongly related to the frequency they operate on. Frequencies in the upper VHF and lower UHF regions are therefore very attractive for mobile military tactical networks. Due to the large wavelength, the waves can more easily diffract around obstacles than at higher frequencies [1]. Furthermore, the frequency is high enough to allow terminals with multiple antenna elements, at least for vehicular terminals. The absolute bandwidth available for a communication system in this frequency range is, however, quite limited. Thus, to meet the demands for high data rates, spectral efficiency is very important. Communication systems with multiple antennas at both the transmitting and receiving side, so called multiple-input multiple-output (MIMO) communication systems, are a very promising way to achieve this. In fading environments, MIMO systems have shown to offer a large capacity increase over single-input single-output (SISO) systems [2–4]. In theory the capacity increases linearly with the minimum of the number of Tx and Rx antennas. However, in real environments, the achievable capacity depends on the radio-channel characteristics.

In order to design and evaluate MIMO systems for tactical communication networks, relevant and realistic channel models are required. However, no suitable peer-to-peer MIMO channel models exist for frequencies around 300 MHz. Most of the MIMO channel measurements and proposed models in the literature are for significantly higher frequencies (mostly 2 and 5 GHz) typically for cellular and personal wireless communication systems. In [5], an overview of such work is given. Measurements of angular properties is analyzed for a peer-to-peer scenario at 1.9 GHz in [6]. Analysis of achievable

capacities and wideband characteristics for peer-to-peer MIMO scenarios at 2.5 GHz are presented in [7] and [8]. For SISO systems, measurements and analyses have been conducted for lower frequencies. For example, narrowband measurements have been performed at 400 MHz for design and evaluation of the TETRA system [9, 10]. Path loss investigations in an urban environment for tactical systems at 225, 450 and 900 MHz are presented in [11]. Furthermore, [12] reports wideband measurements at 400 MHz, and in [13], the feasibility of wideband, spectrally efficient MIMO peer-to-peer communications is demonstrated at 456, 904, and 2177 MHz. Moreover, double-directional channel measurements at 300 MHz, in a semi-rural and suburban environment, are presented in [14].

In this report we present results from a MIMO measurement campaign at 300 MHz in an urban environment in Malmö, Sweden. This measurement campaign is similar to the one earlier performed in Linköping. The results from Linköping is reported in [15]. This report is outlined in the same way as [15]. Also, the body text of both the reports are partly overlapping. The scenarios in this report are peer-to-peer and base station scenarios. In [15], it is only a peer-to-peer scenario. The MIMO channel was measured along 23 Rx routes, with a total length of about 10 km, for 2 different receiver locations. In the analysis we focus on basic channel characteristics, which are important for the development and validation of realistic channel models. Specifically, we investigate the distance dependency of the path loss, the distributions for the large-scale fading, the Ricean $K$-factor, delay spread, and the ergodic capacity (evaluated at a fixed signal-to-noise ratio (SNR)). Furthermore, the difference between the local (per measured route) distributions and the global distributions (for the scenario) is studied. In addition, the correlation distance of the parameters is examined. Moreover, we analyze the correlation between the channel parameters, as well as the correlation between capacity and the channel parameters.

The report is organized as follows; in Chapter 2, the measurements are described. The scenario is presented together with a brief description of the measuring equipment and the data processing. In Chapter 3, the estimation of the channel characteristics are described theoretically. The characteristics treated are: path gain, path-gain model, large-scale fading, $K$-factor, RMS delay spread, capacity, correlation distance for some parameters, and correlations between different channel parameters. The results from the analyzes are presented in Chapter 4, where the channel characteristics described in the preceding chapter are estimated from the measured data. The distributions are studied and the difference between the local (per measured route) distributions and the global distributions (for the scenario) is also studied. Finally, the conclusions are given in Chapter 5.

# 2 Measurements

This chapter starts with a description of the measurements scenario in Malmö. Then a brief description of the measurement equipment is given together with some references to more thorough descriptions. Before an analysis of channel characteristics is made, measured data has to be averaged and processed, which also is described in this chapter.

## 2.1 Measurements Scenario

The measurement campaign was performed in the city center of Malmö, which is the third largest city in Sweden with about 285000 inhabitants. Figure 2.1 shows an aerial photo of the measurement area. This area of the town, which typically has five- to ten-story buildings, has a mix of house blocks, streets, squares, and parks. In the figure, measurement routes 14–19 can be seen (yellow arrows). The other routes are within the area marked by the yellow dashed line. This smaller area is shown in more detail in Figure 2.2, where the other routes, i.e. routes 1–13 and 20–23, are marked by red and blue arrows.

The measured scenario consists of two different transmitter (Tx) locations and 23 receiver (Rx) routes (19 for Tx location 1 and 4 for Tx location 2). During the measurements, the Tx was stationary at each site, while the Rx was driven along the measurement routes. The two Tx sites are in the following referred to as Tx1 and Tx2, respectively. Tx1 is located at the roof of a parking house near a river to the north. Tx2 is close to a park with tall trees (about 20 m in height). Thus, the measurement campaign involves two scenarios:

- Tx1 represents an elevated scenario
- Tx2 represents a peer-to-peer scenario

The Tx1 scenario is called elevated as it is not a good example of a base station scenario. For Tx1, the transmitter with a height of about 1.8 m (the transmitter is mounted on a roof of a car) is placed at a large flat roof of a parking house. This is not a typical base station scenario for which the transmitter would be placed much heigher above the roof than 1.8 m.

The length of the routes, which are shown in Table 2.1, varies considerably as their start and stop positions were chosen to obtain as straight lines as possible, with easily identifiable references in the environment.

LOS, or near LOS, conditions are rare in the measurement area for Tx1, but there are exceptions. For example, for Tx1 there is LOS, or almost LOS, at the end of Route 1, whole Route 3, at the end of Route 7, and at the beginning of Route 11. For Tx2, there is LOS for Routes 20 and 23. For Route 21 of Tx2


Figure 2.1: Measurement area with transmit sites (red rings) and receiver routes 14–19 (yellow arrows). Receiver routes 1–13 and 20–23 are within the yellow dashed area.

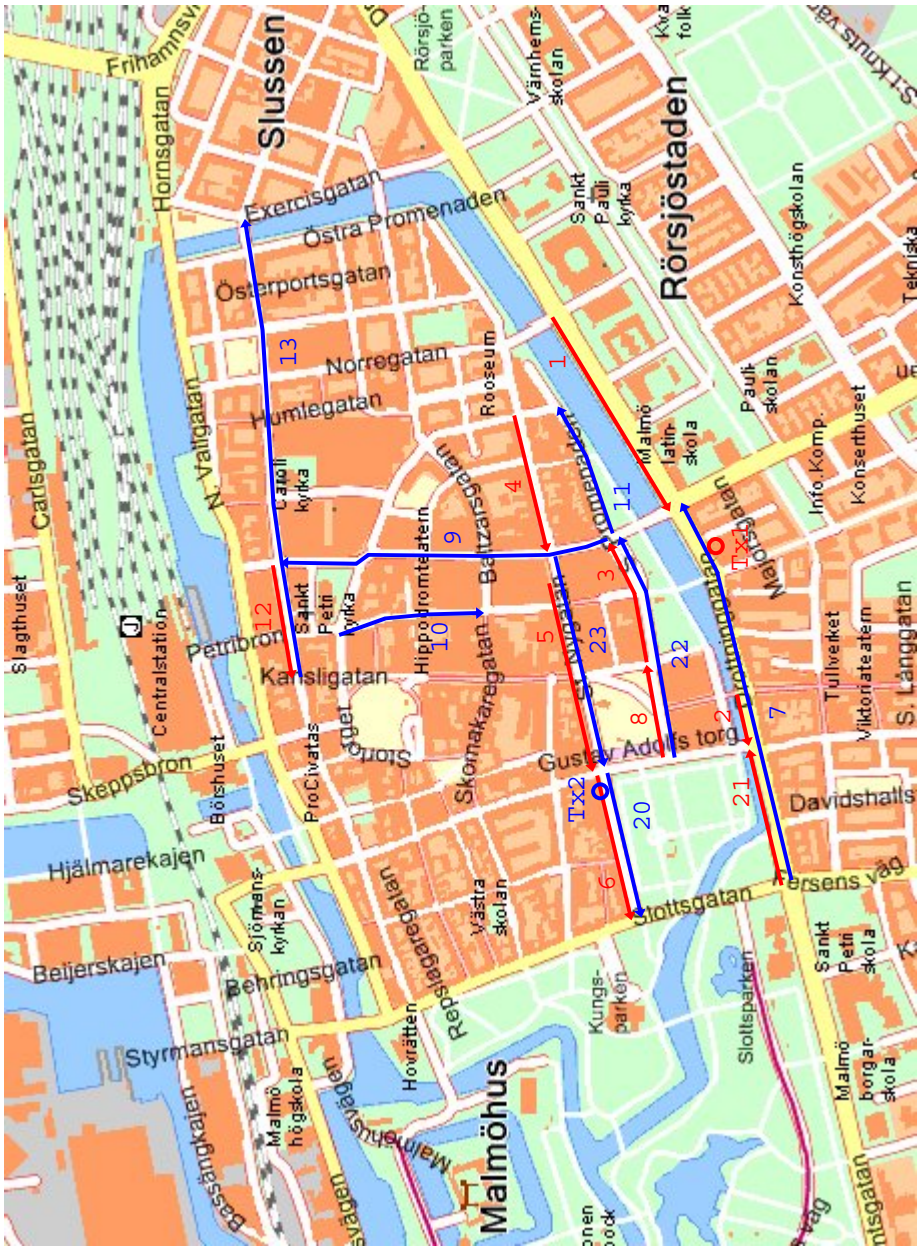


Figure 2.2: The smaller part of the measurement area with transmit sites (rings) and receiver routes 1–13 and 20–23.

| Route No. | Route length (m) | |
|---|---|---|
| | Tx1 | Tx2 |
| 1 | 341 | - |
| 2 | 71 | - |
| 3 | 240 | - |
| 4 | 255 | - |
| 5 | 339 | - |
| 6 | 241 | - |
| 7 | 665 | - |
| 8 | 156 | - |
| 9 | 510 | - |
| 10 | 231 | - |
| 11 | 225 | - |
| 12 | 116 | - |
| 13 | 711 | - |
| 14 | 698 | - |
| 15 | 964 | - |
| 16 | 520 | - |
| 17 | 891 | - |
| 18 | 691 | - |
| 19 | 871 | - |
| 20 | - | 222 |
| 21 | - | 217 |
| 22 | - | 380 |
| 23 | - | 356 |

Table 2.1: Length of the receiver routes in meters.

Figure 2.3: Antenna array with 8 elements.

there are no obstructing buildings. However, for this route, there is vegetation with tall trees obstructing the direct path.

## 2.2 Measuring Equipment

Measurement data were recorded with the RUSK-LUND MIMO channel sounder, which sequentially measures the channel between all combinations of transmit and receive antenna elements within a short time interval. (For a description of the measurement principle, see [16, 17].) The measurements were performed at a center frequency of 285 MHz and with a bandwidth of 20 MHz. The transmitter output power was 43 dBm and the sounding signal was a 12.8 $\mu$s long, periodically repeated, spreading sequence. Thus, the spectrum of the 20 MHz wide probing signal consists of 257 frequency lines, separated by 78.125 kHz. Since the antenna element switching takes place every second period of the probing sequence, delays up to 12.8 $\mu$s could be measured unambiguously; which was more than sufficient in this environment. One full switching cycle, which takes about 1.8 ms, constitutes a channel snapshot.

The transmitter and receiver were equipped with identical 8 element antenna arrays. The array type could be characterized as a vertically polarized, 7 element uniform circular dipole array (UCDA), with a radius of about 0.6 meter. One additional center element is located in an elevated position with respect to the other elements. Furthermore, the 7 UCDA elements are positioned in front of a cylindrical metallic reflector, giving each of the 7 elements a directional radiation pattern. A picture of the antenna array is found in Figure 2.3.

The transmitter and receiver vehicles are shown in 2.4 where the car to the right is the receiver vehicle. The heights for the antennas mounted on the cars are about 1.8 m for the transmitter and about 2.1 m for the receiver. For the peer-to-peer scenario (the Tx2 scenario), this are the antenna heights used in the measurements. For the elevated scenario (the Tx1 scenario), the transmitter car is located at a roof of a building resulting in a height of about 17-20 m.

The data recording was controlled by pulses from an odometer mounted on one of the wheels on the receiver vehicle. The distance between the pulses was about 0.25 m. At each trigger event, one data block of 4 channel snapshots were recorded. Considering that the speed during the measurements never exceeded 10 m/s (mostly just a few m/s), the channel could be assumed to be static during one data block. (At 10 m/s the movement would be 18 mm during one snapshot.)


Figure 2.4: Antenna arrays mounted on transmitter (to the left) and receiver (to the right) vehicles.

## 2.3 Data processing

One snapshot consists of a channel transfer function that is obtained by comparing each frequency line in the measured data with the corresponding response in the data recorded during system calibration. The result for snapshot $k$ is a channel transfer matrix estimate $\widetilde{\mathbf{H}}_k$ of size $n_{\mathrm{Rx}} \times n_{\mathrm{Tx}}$, where $n_{\mathrm{Rx}}$ and $n_{\mathrm{Tx}}$ are the number of Rx and Tx elements, respectively. Each element of $\widetilde{\mathbf{H}}_k$ contains the complex-valued frequency transfer function at the measured 257 spectral lines.

To increase the SNR, the snapshots within each recorded data block was coherently averaged. This implies that the channel is assumed to be approximately static over the 4 snapshots. The averaging process will increase the SNR by 6 dB. The noise level was estimated to correspond to a transfer function of about -138 dB after the SNR enhancement. The output of the data processing is a series of channel transfer matrices $\mathbf{H}_m = \frac{1}{4}\sum_{k=0}^{3} \widetilde{\mathbf{H}}_{4m+k}, m \in [1, M]$, where $M$ is the number of data blocks recorded on a route.

From the channel transfer function a number of different channel characteristics can be estimated.

# 3 Estimation of Channel Parameters

In order to statistically characterize the measured radio channel, a number of scalar parameters describing various channel characteristics are extracted from the measured data. This chapter introduces the channel parameters and describes the estimation techniques.

The first parameter discussed is the path gain, which is followed by a presentation of the model for the geometrical distance dependency of the path gain. This model is in a later step used to extract the large-scale fading from the measured path gain. The chapter proceeds with a description of the estimator for the Ricean $K$-factor, which characterizes the small-scale fading of the channel, and the estimator for the RMS delay spread, which is used to quantify the delay-spread properties of the channel. This is followed by a definition of the narrowband channel capacity estimator. Finally, the estimation of the correlation between different channel parameters and the correlation distances for the parameters are described.

## 3.1 Path Gain

The path gain (reciprocal of path loss) $G = P_R/P_T$, with $P_R$ and $P_T$ denoting the received and transmitted power, respectively, was calculated for all positions along the measured routes by averaging the squared magnitudes of the transfer function over all frequency subchannels, and over all combinations of transmitter and receiver antenna elements. Due to the large diversity order achieved, no significant fast fading could be observed.

Finally, the path gain was averaged over 4 consecutive spatial data blocks, thus providing a result $G_{\mathrm{meas}}$ for approximately every 1 m along the route. As an example, the measured path gain for Route 9 and transmitter position 1 is shown in Figure 3.1.

## 3.2 Path-Gain Model

The path gain between transmitter and receiver depends on a number of different factors, for example the distance between transmitter and receiver, the presence of objects blocking the LOS component, or reflections from objects in the surrounding resulting in multi-path propagation.

The distance-dependent part of the path gain can be modeled as a function

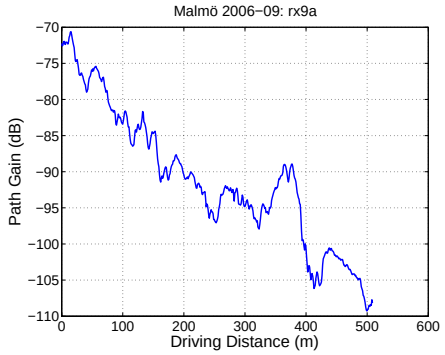


Figure 3.1: Measured path gain for Route 9.

of the geometrical distance $d$

$$G(d) = G_0 - 10n \log_{10} \left(\frac{d}{d_{\text{ref}}}\right), \quad [\text{dB}] \tag{3.1}$$

where $G_0$ is the path gain at the reference distance $d_{\text{ref}}$ and $n$ is the path gain exponent.

## 3.3 Large-Scale Fading

The large-scale fading along the measured routes is computed by removing the distance dependent part of the path gain (3.1) from the measured path gain $G_{\text{meas}}$ as

$$G_{\text{LS}}(r) = G_{\text{meas}}(r) - G(d(r)), \quad [\text{dB}] \tag{3.2}$$

where $r$ is the driving distance along the route and $d$ is the geometrical distance between Tx and Rx. Since the distance dependent part of the total path gain has been removed, we may assume that the large scale fading process $G_{\text{LS}}$ is more stationary than $G_{\text{meas}}$. The stationarity can be checked, e.g., by comparing the mean and standard deviation of $G_{\text{LS}}$ for each route.

In order to obtain a zero-mean fading process, we define

$$\widetilde{G}_{\text{LS}}(r) = G_{\text{LS}}(r) - \overline{G}_{\text{LS}}, \quad [\text{dB}] \tag{3.3}$$

where $\overline{G}_{\text{LS}}$ is the per route and Tx position mean value of $G_{\text{LS}}$. This zero-mean process is expected to be more stationary and vary less than $G_{\text{LS}}(r)$.

## 3.4 K-factor

According to the standard modeling, where the received signal is a composition of a non-fading component and a Rayleigh fading component, the received signal envelope is Ricean distributed. The physical interpretation is that the non-fading part is due to a LOS (or quasi-LOS) propagation path, and that the Rayleigh distributed part is a result of a large number of scattered signal components adding up. The $K$-factor is defined as the ratio between the power of the non-fading component and the power in the Rayleigh fading signal component. A $K$-factor equal to zero corresponds to a Rayleigh fading signal envelope, and a large $K$-factor indicates the non-fading (LOS) component to be dominating. Hence, the $K$-factor can be viewed as a measure of how close to LOS a propagation scenario is. However, it should be noticed that a non-fading signal component can be due to other propagation mechanisms than LOS (e.g., diffraction and specular reflection).

The small-scale fading characteristics in our measured scenario was investigated by studying the propagation channel between the two (horizontally omnidirectional) center elements of the arrays. By exploiting the in-phase and quadrature-phase (I/Q) components, the $K$-factor estimation performance can be significantly improved [18–20] compared to methods based on fading envelop statistics only. Common to these I/Q estimators is that they find the amplitude of the non-fading signal component from the largest peak in the Doppler spectrum. In our analysis we use the estimator proposed in [20],

$$\hat{K} = \frac{1}{N}\left[(N-2)\frac{\hat{A}^2}{\hat{\Omega}-\hat{A}^2} - 1\right], \tag{3.4}$$

where $\hat{A}$ is an amplitude estimate of the non-fading signal component, $\hat{\Omega}$ an estimate of the total signal power and $N$ is the sample size.

Due to the large wavelength ($\approx$1 m) in our measurements, it was not possible to obtain samples from the spatial domain only and at the same time maintain a reasonable spatial resolution. Instead, $\hat{A}$ was estimated from the largest peak in the joint delay-Doppler spectrum, based on all frequencies and four consecutive (spatial) data blocks[1]. The total power estimate, $\hat{\Omega}$, was computed from the squared magnitudes of the frequency transfer function over the 4 blocks.

[1] An initial coarse estimate was computed by a two-dimensional fast Fourier transform (FFT) of the complex transfer function over the 257 frequency subchannels and over four consecutive (spatial) data blocks; using a zero-padding factor of two in each dimension. This initial estimate was then refined iteratively 12 times, where the resolution (in each dimension) was increased by a factor two for each iteration.

It can be pointed out that this $K$-factor estimator, even in situations when the Ricean fading assumption is not fulfilled, has an attractive physical interpretation. For large $N$, the estimate is the power relation between the strongest signal in the delay-Doppler spectrum and the received power in all other signal components. It is, however, due to a limited observation windows in frequency and space, no guarantee of that $\hat{A}$ is only representing a single physical propagation component.

The above mentioned interpretation of $\hat{K}$ can be compared with the LOS power factor, $K_{\mathrm{LOS}}$, proposed in [21], which is the relation between the power in the LOS component, identified from a double-directional channel characterization [22], and the power in all other components. Since the strongest component used in $\hat{K}$, not necessarily corresponds to the LOS component, $K_{\mathrm{LOS}}$ and $\hat{K}$ may differ.

## 3.5 RMS Delay Spread

The power delay profile (PDP) (also commonly referred to as the power delay spectrum) is computed by averaging the power in the channel impulse responses over all spatial channels. The impulse responses are obtained by a discrete inverse Fourier transformation (IFFT) of the complex frequency transfer functions. To reduce the side-lobe levels, a Blackman window is applied on the frequency data before the transformation. Averaging over four consecutive PDPs reduces the variance and gives one resulting PDP $P(\tau)$ for about every meter along the measured routes.

The root-mean-square (RMS) delay spread, which is defined as the square root of the second central moment of the PDP [23], is computed as

$$\sigma_\tau = \sqrt{\frac{\sum_i (\tau_i - \overline{\tau})^2 P(\tau_i)}{\sum_i P(\tau_i)}}, \tag{3.5}$$

where $\tau_i$ is the delay for delay bin $i$ and $\overline{\tau}$ is the mean delay

$$\overline{\tau} = \frac{\sum_i \tau_i P(\tau_i)}{\sum_i P(\tau_i)}.$$

Here, $P(\tau_i)$ denotes the power in the delay bins (from the IFFT) that exceeds a certain threshold above the background noise. The background noise level in each profile is estimated from a continuous portion of the profile at the start, before the first signal component arrives, or at the end when all signal components has decayed.

## 3.6 Capacity

The narrowband ergodic MIMO channel capacity for a transmitter without channel state information is given by [3]

$$C = E\Big\{\log_2 \det\Big(\mathbf{I} + \frac{\gamma}{n_{\mathrm{Tx}}}\mathbf{H}\mathbf{H}^*\Big)\Big\}, \tag{3.6}$$

where $\det(\cdot)$ is the determinant operator, $(\cdot)^*$ the Hermitian transpose, $n_{\mathrm{Tx}}$ the number of transmit antennas, $\gamma$ the SNR, and $\mathbf{I}$ is the identity matrix. $\mathbf{H}$ is normalized such that the expected value of its squared Frobenius norm $E\{\|\mathbf{H}\|_F^2\} = n_{\mathrm{Rx}}n_{\mathrm{Tx}}$, where $n_{\mathrm{Rx}}$ is the number of receive antennas. In our capacity evaluation, the expectation in (3.6) was taken over the measured 257 frequency subchannels and over 4 consecutive (spatial) data blocks.

## 3.7 Correlations

The correlation between the different channels parameters is an important property when constructing and evaluating channel models. For a channel model to be considered relevant it needs not only to generate channels that have realistic distributions, but also that have realistic correlations between them.

The correlation coefficient $\rho_{X,Y}$ between two random variables $X$ and $Y$ with expected values $\mu_X$ and $\mu_Y$ and standard deviations $\sigma_X$ and $\sigma_Y$ is defined as:

$$\rho_{X,Y} = \frac{\mathrm{cov}(X,Y)}{\sigma_X\sigma_Y} = \frac{E([X-\mu_X][Y-\mu_Y])}{\sigma_X\sigma_Y}, \tag{3.7}$$

where cov means covariance.

## 3.8 Correlation Distance

The correlation of a channel parameter between two separated points along the route is an important property of a channel model. The distance autocovariance function for a channel parameter $X$ is

$$R_r(\Delta r) = E\{(X(r)-\mu_X)(X(r+\Delta r)-\mu_X)\}, \tag{3.8}$$

where $\mu_X$ denotes the expected value of X. The distance correlation function is the autocovariance function normalized by the autocovariance function for zero-lag,

$$\rho_r = R_r(\Delta r)/R_r(0). \tag{3.9}$$

In our analysis we define the correlation distance as the smallest (non-negative) distance $\Delta r$ for which $\rho_r(\Delta r) \leq 0.5$. The autocovariance function (3.8) is computed with the unbiased estimator

$$\hat{R}_r(\Delta r) = \hat{R}_r(k\delta_r) = \frac{1}{N-k} \sum_{n=1}^{N-k} \left(X(r_n) - \overline{X}\right) \left(X(r_{n+k}) - \overline{X}\right), \quad (3.10)$$

where $\delta_r$ is the equidistant sampling interval along the route and

$$\overline{X} = \frac{1}{N} \sum_{n=1}^{N} X(r_n),$$

is the sample mean of $X$.

Great care should be exercised considering this autocovariance estimator. The stationary condition is not always met in field experiments with mobile units and for short routes (small $N$), the number of terms in the estimator ($N - k$) can be very small if $k$ is large. In the latter case, a biased estimator might be more reliable. However, for small values of $k$ compared to $N$, and under reasonably stationary conditions, the estimator (3.10) could be expected to work quite well.

# 4 Results

In this chapter we investigate the distance dependency of the path loss, the distributions for the large-scale fading, the Ricean $K$-factor, delay spread, and the ergodic capacity (evaluated at a fixed SNR). Furthermore, the difference between the local (per measured route) distributions and the global distributions (for the scenario) is studied. In addition, the correlation distance of the parameters is examined. Moreover, we analyze the correlation between the channel parameters, as well as the correlation between capacity and the channel parameters.

## 4.1 Path Gain

The cumulative distribution function (CDF) for the mean path gain (computed as described in Sec. 3.2) is presented in Figure 4.1(a) for the two Tx locations. The geometrical distances can be divided into 2 groups, one with distances of a few hundred meters (Route 1–13 and 20–23) and one with distances 1–3 kilometers (Route 14–19); see maps in Figure 2.1 and 2.2. In Figure 4.1(b), the mean path gain for all routes and Tx combinations is shown as a scatter plot vs. the geometrical distance.

## 4.2 Path-Gain Model

The two parameters $G_0$ and $n$ in the path-gain model (3.1) are estimated by regression analysis of the mean path gain (expressed in dB) from the measured data (a minimum square error fit of the model). To maintain a dataset that spans a reasonable large interval of geometrical distances, it was not considered feasible to estimate model parameters per route, as the range of distances for many of the routes (especially those almost orthogonal to the LOS path) is very limited. Thus, all data (all Tx–Route combinations) were combined. From the regression analysis, the values of the parameters are found to be $G_0 = 17.54$ dB and $n = 4.55$ for a reference distance of 1 m. The distance-dependent path gain derived from this model is shown by the solid red line in Figure 4.1(b). Interestingly, the value for the path gain exponent is quite close to 4, which is what is obtained from a flat-earth model [1] . It should however be noted that the flat-earth model lacks physical relevance in the measured scenario. When using

[1]The path gain (in linear power scale) for a simple flat-earth (two-ray) model [23] is $G_{\mathrm{FE}} = (h_{\mathrm{Tx}} h_{\mathrm{Rx}})^2 / d^4$, where $h_{\mathrm{Tx}}$ and $h_{\mathrm{Rx}}$ are the Tx and Rx antenna heights, respectively.

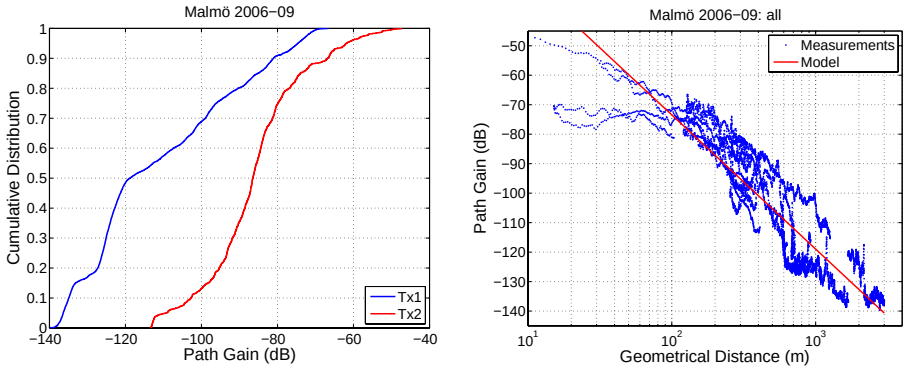


Figure 4.1: Path gain. (a) CDFs for the two Tx sites. (b) All measurements vs. geometrical distance; the fitted model shown as a red solid line.

the estimated parameters in (3.1), the resulting model is

$$G(d) = 17.54 - 10 \cdot 4.55 \cdot \log_{10}(d). \quad [\text{dB}] \tag{4.1}$$

In Figure 4.2, the measurements are compared to the resulting model for each transmitter position. The values of $G_0$ and $n$ are for Tx1 17.68 dB and 4.56, respectively, and for Tx2, 14.37 dB and 4.41, respectively. The reason for separately fit parameters for the two sites is that Tx1 is located at the roof of a parking house and Tx2 at street level, i.e. two different scenarios. Thus, for Tx1 and Tx2, the resulting models are

$$G(d) = 17.68 - 10 \cdot 4.56 \cdot \log_{10}(d) \quad [\text{dB}] \tag{4.2}$$

and

$$G(d) = 14.37 - 10 \cdot 4.41 \cdot \log_{10}(d), \quad [\text{dB}] \tag{4.3}$$

respectively.

The measured path gain is plotted as a function of the geometrical distance. It can be noted that, for the most part, the measurements are for geometrical distances shorter than 1000 meters. The mean geometrical distance is 934 meters for Tx1 and 220 meters for Tx2. The overall mean of the geometrical distance is 849 meters. From a channel modeling point of view it would be preferable to have a similar (ultimately uniform) distribution of geometrical distances from all the transmitter positions, especially if the propagation conditions vary between the sites. However, this is not always possible when conducting measurements. For instance, route Rx7 is set apart from the others as it passes by

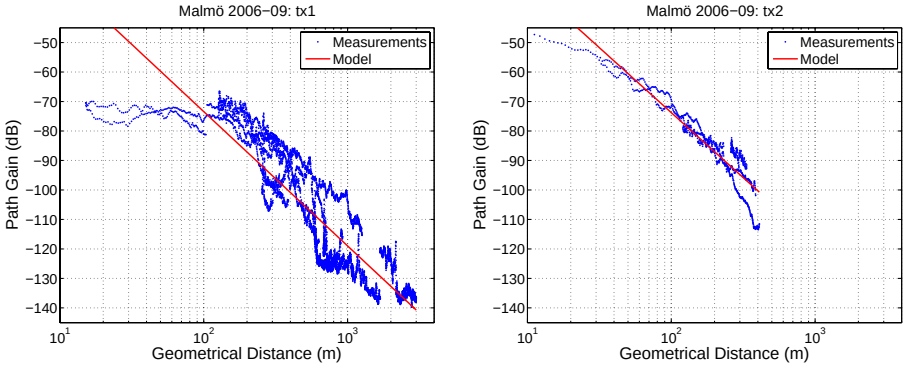


(a) (b)

Figure 4.2: Measured path gain vs. geometrical distance for the two Tx sites. The model fitted separately to data of each Tx site is shown as a solid red lines.

close to the transmitter (about 15 m when closest). This route is clearly visible in Figure 4.1(b) and 4.2(a), that is, the route that gives a measured path gain clearly belowe that of the model. One reason for the poor agreement is that the flat-earth (two-ray) model is not valid for short geometrical distances. Thus, there is a reason for removing route Rx7. On the other hand, one route will not affect the overall result.

## 4.3 Large-Scale Fading

The large-scale variations $G_{\mathrm{LS}}$ of the path gain are obtained by subtracting the distance-dependent path gain (4.2) for Tx1 and (4.2) for Tx2 from the measured mean path gain (in dB) according to (3.2). As an example, Figure 4.3(a) shows $G_{\mathrm{meas}}(r)$ and $G(d(r))$ along Rx9 for Tx1. Here, the large-scale fading is always positive. From the distribution for $G_{\mathrm{LS}}(r)$ for all routes, shown in Figure 4.3(b), we see that the variation around the distance-dependent model is about $\pm 15$ dB, with a mean standard deviation of about 9 dB for all Tx positions together (9.48 dB for Tx1 and 4.99 dB for Tx2).

A closer examination of the geometrical distance dependency of the path gain, where each Tx–Route combination could be identified, reveals that most Tx–Route pairs have an offset relative $G(d(r))$, and that this offset more or less is maintained along each route. An example illustrating this is given in Figure 4.4, which shows the measured mean gain on Rx9 for Tx1, as well as the modeled gain in (4.2), against the geometrical distance. Here, the offset between the mean large-scale fading and the model is about 9.8 dB, which, in

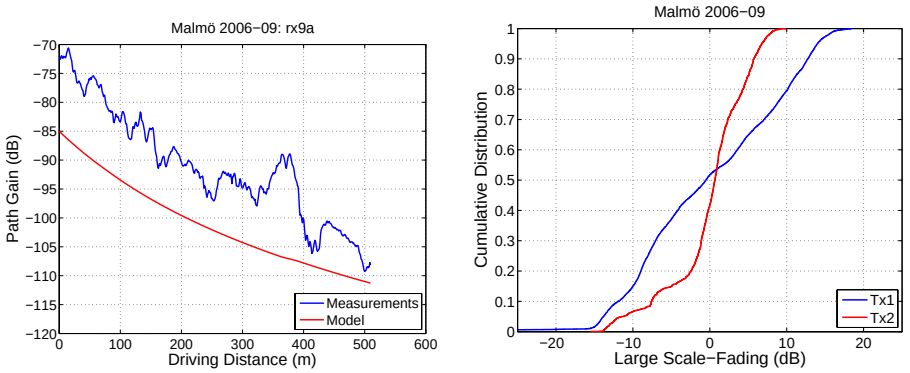


Figure 4.3: (a) Measured mean path gain and modeled path gain along Route 9 for Tx1. (b) CDF for the large-scale fading from each Tx.

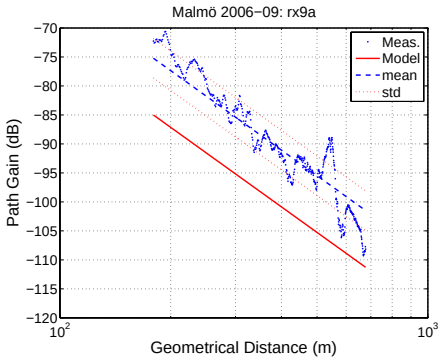


Figure 4.4: Measured path gain vs. geometrical distance.

fact, is larger than the variations around the local mean (blue dashed line).

This non-stationary behavior is investigated further by computing $\overline{G}_{\mathrm{LS}}$ and $\overline{\sigma}_{G_{\mathrm{LS}}}$, the per route and Tx position mean and standard deviation of $G_{\mathrm{LS}}(r)$. The CDFs for this "local" statistics are given in Figure 4.5 for each Tx position separately. The CDFs show that $\overline{G}_{\mathrm{LS}}$ varies about $\pm 14$ dB for the different routes, and that $\overline{\sigma}_{G_{\mathrm{LS}}}$ has a median value of 3 dB; see also Figure 4.6. Considering all transmitters, the observed distribution for $\overline{G}_{\mathrm{LS}}$ is close to uniform.

From the observations above, it can be assumed that the zero-mean fading process $\widetilde{G}_{\mathrm{LS}}(r)$ in (3.3) obtained by removing $\overline{G}_{\mathrm{LS}}$ from the large-scale fading

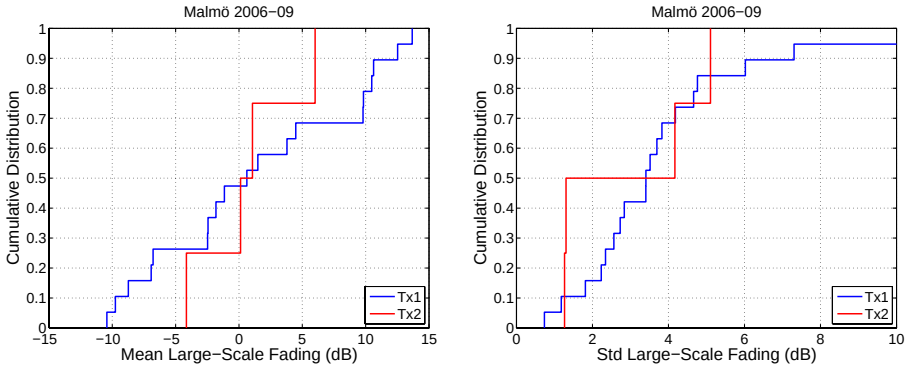


Figure 4.5: Large-scale fading per-route statistics. (a) Mean. (b) Std.

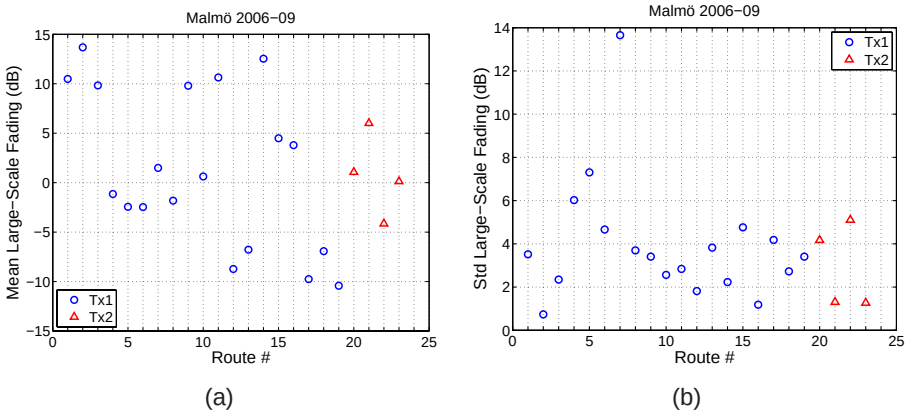


Figure 4.6: Per-route statistics for the large-scale fading. (a) Mean. (b) Std.

variations for each route and Tx combination, would be more stationary and vary less than $G_{\mathrm{LS}}(r)$. The CDF for $\widetilde{G}_{\mathrm{LS}}(r)$ is shown in Figure 4.7(a) for each Tx position. The distributions are not similar, which most likely is due to the fact that Tx1 is located at the roof of a parking house and Tx2 at street level. The standard deviations for Tx1 and Tx2 are 5.25 dB and 3.53 dB, respectively. Comparing these distributions with those for $G_{\mathrm{LS}}$ in Figure 4.3(b), it is clear that the large-scale fading within the "local" per-route environments are significantly less than what is obtained for the global scenario.

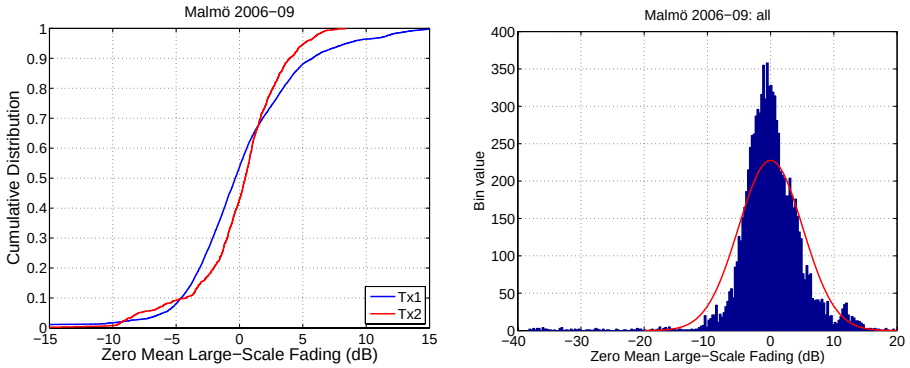


Figure 4.7: Distribution for the large-scale fading zero-mean process $\widetilde{G}_{\mathrm{LS}}(r)$. (a) CDF. (b) Histogram for all Tx positions. In addition, the solid red curve shows a normal distribution with the same variance.

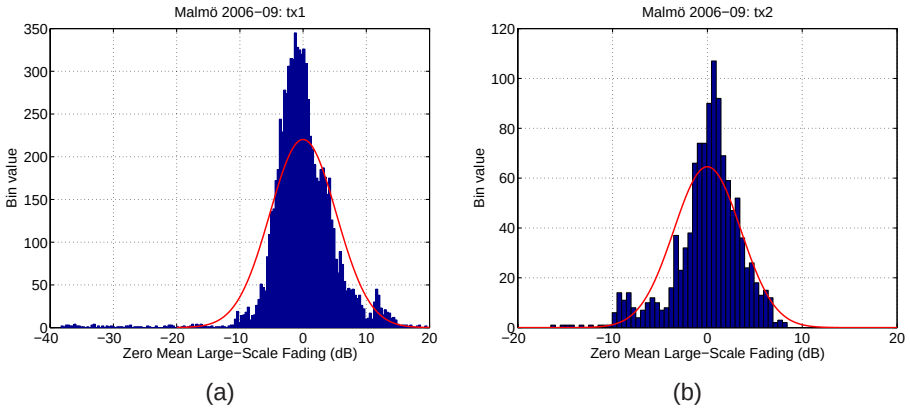


Figure 4.8: Histogram of the zero-mean process, for each transmitter position.

The histogram for the distribution of $\widetilde{G}_{\mathrm{LS}}(r)$ for all Tx positions combined is shown in Figure 4.7(b), where the probability distribution function (PDF) for a normal distribution with the same variance also is shown by the solid red curve. (The PDF in the figure is scaled with the total number of measurements and the bin width of the histogram.) The figure shows that $\widetilde{G}_{\mathrm{LS}}(r)$ is fairly close to normally distributed. The histograms for the individual Tx positions are shown in Figure 4.8.

The correlation distance of $G_{\mathrm{LS}}(r)$ is an important statistical property of

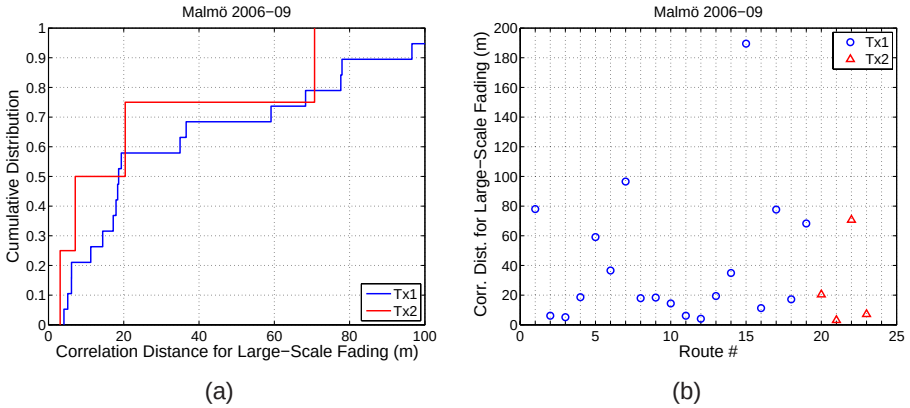


Figure 4.9: Correlation distance for the large-scale fading $\widetilde{G}_{\mathrm{LS}}(r)$. (a) CDF. (b) Per route.

the large-scale fading process. The correlation distance function is calculated from (3.9) with the correlation distance defined as the distance where $\rho_r(\Delta r) = 0.5$. The CDF of the correlation distance is presented in Figure 4.9(a) for the two Tx positions.

The distributions for the positions are similar with the exception of one large correlation distance for Tx1. The mean correlation distances are 41, 25, and 38 m for Tx1, Tx2, and all Tx sites, respectively. In Figure 4.9(b), the measured correlation distances can be associated with the route numbers.

In conclusion, we can model the measured path gain $G_{\mathrm{meas}}$ as the sum of the distance dependent path gain $G_{\mathrm{d}}(d(r))$ in (3.1), the offset $\overline{G}_{\mathrm{LS}}$ that varies from route to route, and the zero-mean fading process $\widetilde{G}_{\mathrm{LS}}(r)$. This model is similar in spirit, though different in the details, to the use of random path-loss coefficients and shadowing variances in [24].

## 4.4 K-factor

The Ricean $K$-factor was computed along the measured routes by the estimator described in Section 3.4. Each estimate is based on four consecutive (non-overlapping) recorded data blocks, which gives an estimate for approximately every 1 m. Before presenting the more general statistics for the $K$-factor, we give some examples of characteristics and relations to the local environment that have been found to be typical in the scenario.

The first example is given in Figure 4.10(a), which shows the $K$-factor

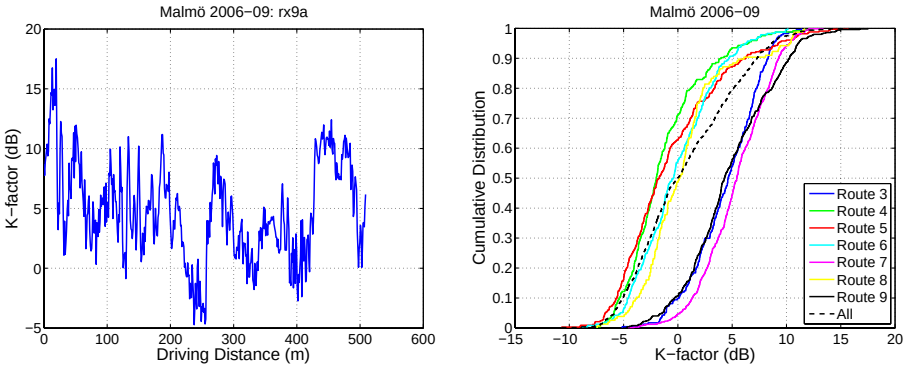


Figure 4.10: (a) Ricean $K$-factor vs. driving distance along Route 9 for Tx1. (b) CDF for the $K$-factors along Route 3-9 for Tx1 and all the seven routes.

along Route 9 for Tx1. We see that the estimate, in general, shows a quite rapid variation along the route. Comparing this plot with Figure 4.3(a), we can see that some of the features in both plots coincides. E.g., the peak in the $K$-factor at about 450 m corresponds to a local maximum in the measured path gain.

The second example is the distributions of the $K$-factors on Route 3–9 for Tx1, which are shown in Figure 4.10(b). The geometrical distance between Tx and Rx on this route is relatively short and the mean value of all seven routes is 308.5 m. The shape of the CDFs do not differ significantly, but the mean value vary among the routes. The CDFs for Route 3, 7 and 9, have a median values that are significantly larger than for the other routes shown. This might be consistent with the interpretation of the $K$-factor as a measure of the "degree" of LOS, as discussed in Sec. 3.4. From the map in Figure 2.2 we see that portions of these three routes are in LOS with respect to Tx1, though LOS occurred very rarely.

The distributions of the $K$-factor from all routes for each Tx position are shown in Figure 4.11. The mean values ($K$ is expressed in dB) are 0.92 and 1.87 dB for Tx1 and Tx2, respectively. The standard deviations are 5.60 respectively 4.97 dB, for the two Tx positions. Taking all Tx positions together, the total mean and standard deviation are 1.03 and 5.54 dB, respectively. A further examination of the distributions reveals that $K$ in Figure 4.11 is, for Tx1, quite close to log-normally distributed. Lognormal distributions of the $K$-factor have been described for cellular scenarios [25] and for peer-to-peer scenarios in [15].

From the CDFs for the individual routes in Figure 4.10(b), we already

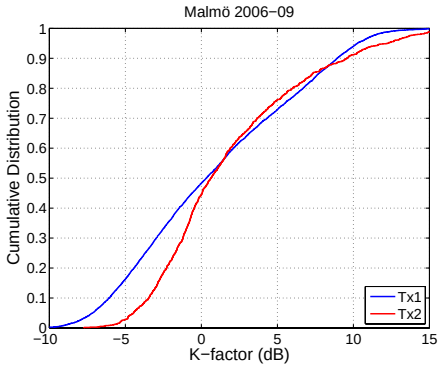


Figure 4.11: CDF for all Ricean $K$-factors measured from each Tx.

observed that the mean values of $K$ differed between the routes. To give an overview of the variations in the "local" statistics, the CDFs of the per-route mean and standard deviation are shown in Figure 4.12. The same statistics are shown in Figure 4.13, but are here plotted for each route and Tx combination, making it possible to associate each value with a specific Route and Tx combination. From these plots it is clear that the per-route mean and standard deviation of the $K$-factor varies considerably. Considering all Tx locations, for the per-route standard deviation, the mean and the standard deviation are 4.08 and 0.85 dB, respectively. Separating Tx1 and Tx2, the values become 4.20 and 0.87 dB for Tx1 respectively 3.94 and 0.88 dB for Tx2.

Removing the per-route mean, $\overline{K}_{\mathrm{dB}}$, from the $K$-factor (in dB), in a similar manner as for the large-scale fading in Section 4.3, we obtain the zero-mean variation $\widetilde{K}_{\mathrm{dB}} = K_{\mathrm{dB}} - \overline{K}_{\mathrm{dB}}$. The CDFs of $\widetilde{K}_{\mathrm{dB}}$ is shown in Figure 4.14. These distributions are more narrow than those for $K_{\mathrm{dB}}$ in Figure 4.11, and have a standard deviation of 3.70 and 3.86 dB, for Tx1 and Tx2, respectively. However, compared to the large-scale fading, the effect of removing the per-rote mean values for the $K$-factor is more modest. This might suggest that the $K$-factor is more dependent on variations in the local environment than the large-scale fading is.

The $K$-factor for the measured scenario in [15] is, in general, very low. This can be explained by the fact that LOS (or close to LOS) conditions rarely exists. Here, Tx1 is placed on a roof, which means a different scenario than in [15]. Thus, LOS is more common in this case, which also gives larger values in the $K$-factor. From Figure 4.13(a), we can identify the routes with the largest mean $K$-factors. For Tx1, Route 1 and 2 (which are close to Tx1) have a mean $K$-

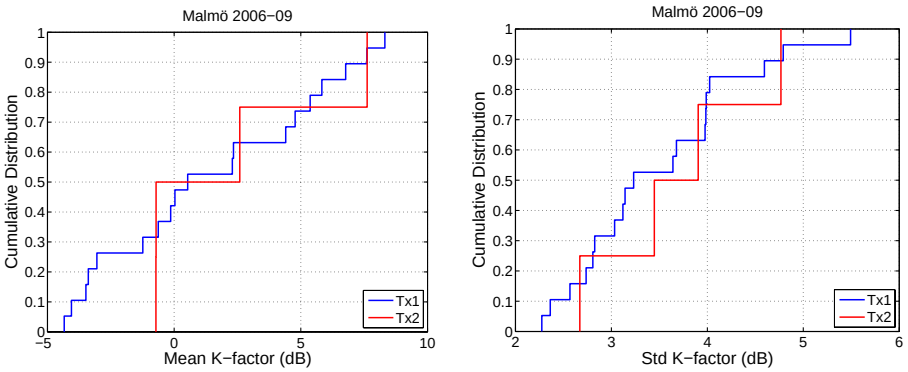


Figure 4.12: CDF of $K$-factor per-route statistics. (a) Mean. (b) Std.

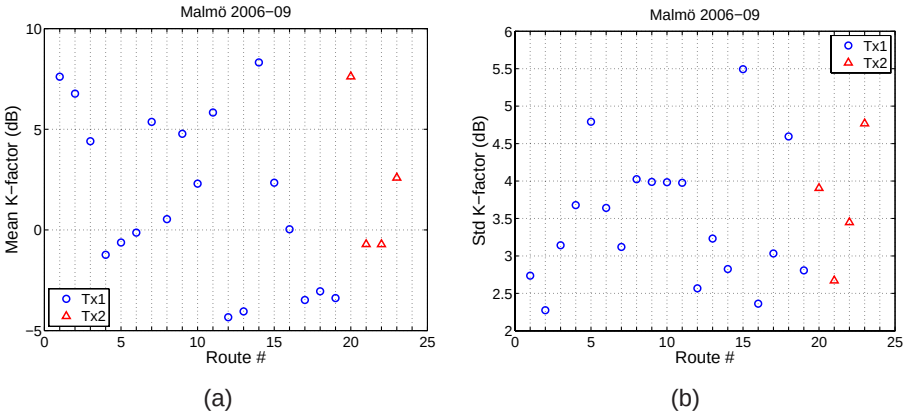


Figure 4.13: Per-route statistics for the $K$-factor. (a) Mean. (b) Std.

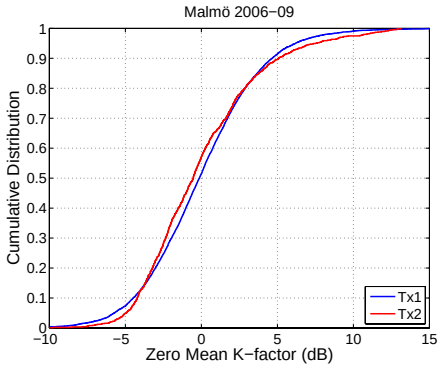


Figure 4.14: CDF for the zero-mean variations $\widetilde{K}_{\mathrm{dB}}$.

factor of 7.61 and 6.77 dB, respectively. Besides these routes, Route 14 has a mean $K$-factor of 8.32 dB. This route is not exactly close to Tx1 but the street is orientated in a direction towards Tx1. Moreover, a large part of this route has no buildings close to the street on one side of the road, as it passes by a park. Along this part, there are, however, large trees on one side of the street. For Tx2, the largest mean $K$-factor is 7.62 dB for Route 20, which passes very close to Tx2. This route is along the same street where Tx2 is placed.

The last analyzed property of the $K$-factor is the correlation distance, which was computed on a per-route basis. The result, in Figure 4.15, shows that the correlation distance for the $K$-factor, in general, is very small. For all Tx positions together, it is less than 5 m for 50% of the routes, and only exceeds 10 m for 26% of the routes.

## 4.5 RMS Delay Spread

### 4.5.1 Delay Spread

The RMS delay spread, $\sigma_\tau$, is computed for about every 1 m along all the measured routes according to the method described in Section 3.5. An example of the estimated RMS delay spread is given in Figure 4.16(a), which shows the delay spread vs. driving distance along Route 9 for Tx1. Comparing this with the measured path gain in Figure 4.3(a) (as we did for the Ricean $K$-factor in Figure 4.10(a)), we again can, to some degree, observe a correlation between the behavior along the route. The peak in the path gain at 450 m corresponds to

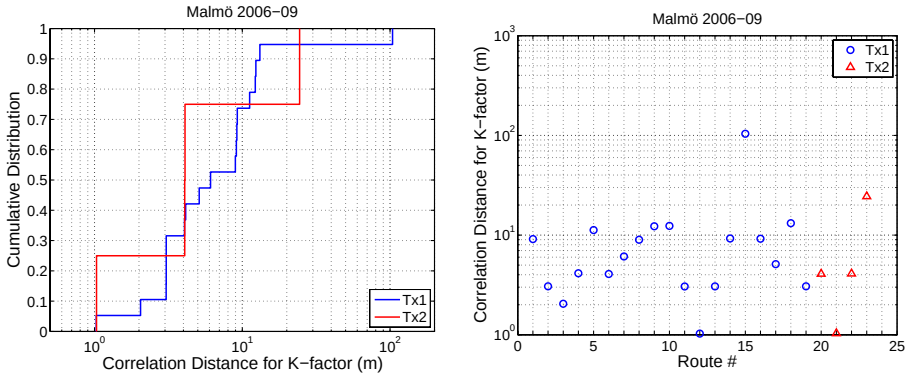


Figure 4.15: Correlation distance for the $K$-factor. (a) CDF. (b) Per route.

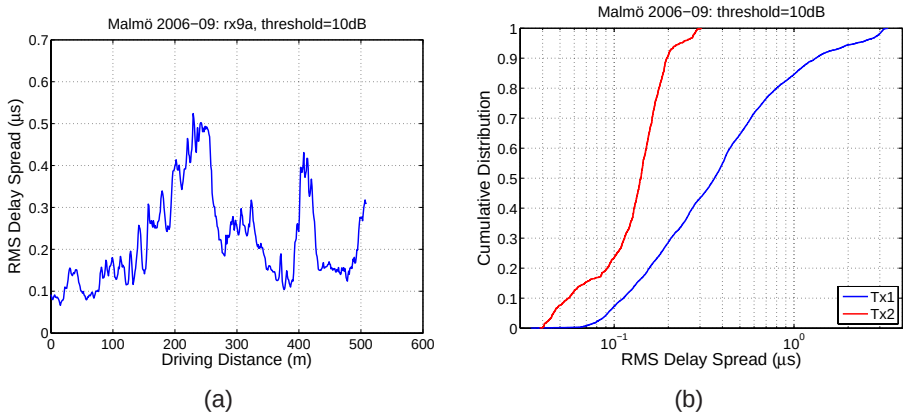


Figure 4.16: RMS delay spread. (a) Delay spread vs. driving distance along Route 9 for Tx1. (b) CDF for all delay spreads measured from each Tx.

a local minimum in the delay spread.

The CDF for the RMS delay spread for all routes is shown in Figure 4.16(b). Considering Tx1, the distribution is close to lognormal. This is in agreement with what has been reported in [26] for a short-range macro-cellular environment at 1.9 GHz. Turning to Tx2, the distribution is not close to lognormal. On the other hand, the Tx2 position consists only of four routes, i.e. Route 20–23. The statistics are simply not good enough to be able to make any statement.

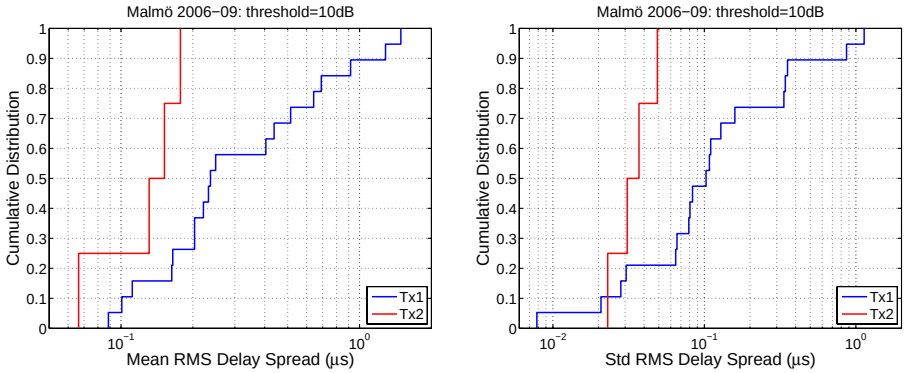


Figure 4.17: RMS delay spread per-route statistics. (a) Mean. (b) Std.

The mean values [2] for Tx1 and Tx2 are 0.37 and 0.13 $\mu$s, respectively. From the distributions of the per-route mean ($\overline{\sigma}_\tau$) and the standard deviation, presented in Figure 4.17, it is clear that there is a large variation between the routes, particularly for the per route mean. Note that these CDFs are based on a linear RMS delay spread. No significant difference was observed for the per route mean using the logarithmically weighted mean. The effects of removing the per-route local mean value, by computing the zero-mean process $\widetilde{\sigma}_\tau = \sigma_\tau - \overline{\sigma}_\tau$, are shown by the CDFs in Figure 4.18(a). For Tx1 and Tx2, the spread have reduced a little. The standard deviation of $\overline{\sigma}_\tau$ is 0.40 and 0.05 $\mu$s, for Tx1 and Tx2, respectively.

Finally, the correlation distance for the RMS delay spread is presented in Figure 4.18(b). The variation between the routes is very large, ranging from 2 m up to almost 116 m, with a median value of about 30 m.

### 4.5.2 Anomalies in the results

In Section 2.2, it is mentioned that the sounding signal was a 12.8 $\mu$s long, periodically repeated, spreading sequence, allowing delays up to 12.8 $\mu$s to be measured unambiguously. Usually, this is sufficient in a built-up environment. However, in Malmö, this was not sufficient for the Tx1 position, which was located at the roof of a parking house. In Figure 4.19(a), the first power delay

[2] Computed as $\exp(\mu)$, where $\mu$ is the mean of $\log(\sigma_\tau)$)

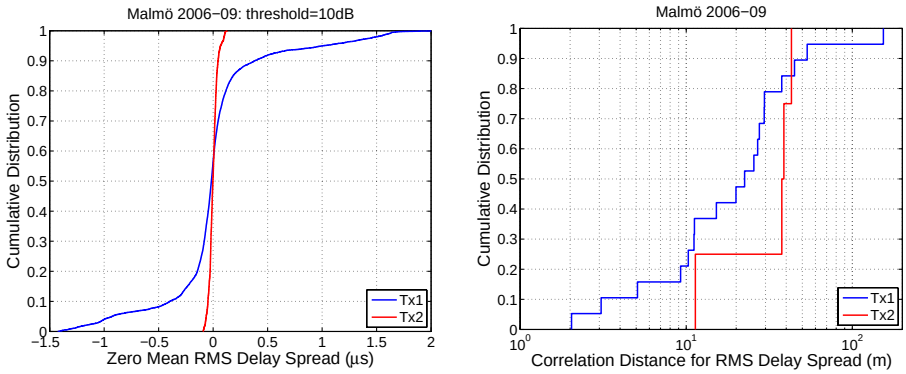


(a) (b)

Figure 4.18: (a) CDF for the RMS delay spread zero-mean process $\widetilde{\sigma}_\tau$. (b) CDF for the RMS delay spread correlation distance.

profile for Route 16 is shown. The geometrical distance for the direct path gives a delay of about 10 $\mu$s. Thus, the two peaks below 5 $\mu$s have to originate from the previous transmitted sequence.

In in Malmö, there is a high bulding called "The Turning Torso". This building is able to return a reflection for, more or less, any transmitter location. When measuring the geometrical distance to this building, one peak or both peaks below 5 $\mu$s would originate from this building, but for the previous transmitted sequence, i.e. we have to shift the delay profile. As all before the direct delay should be noise, everything before it can be shifted. In Figure 4.19(b), we have shifted the delay profile with 6 $\mu$s, resulting in a profile longer than 12.8 $\mu$s.

A reason that reflections from "The turning Torso" are visiable for Route 16 is most likely due to the low signal strength. Route 16 gives the lowest signal strength. For the other routes, no reflections from this building could be identified for certain.

## 4.6 Capacity

The ergodic MIMO capacity is calculated according to (3.6) at a fixed SNR of 10 dB along the measured routes, using the 7 circularly placed elements of the antenna array at both Tx and Rx. Since the capacity is strongly dependent on the rank of the channel matrix, or more precisely the spread of its eigenvalues, the capacity estimates can easily be affected by noise in the data. The sensitivity is higher the lower the numerical rank of the matrix is (i.e., higher for low capacity channels). Therefore, the capacity analysis is only based on measurements that

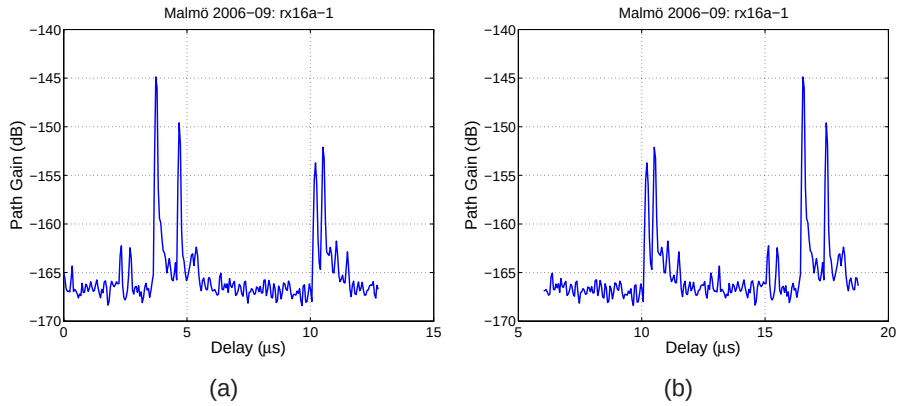


Figure 4.19: First power delay profile for route 16. (a) Raw profile. (b) Profile shifted by 6 $\mu$s.

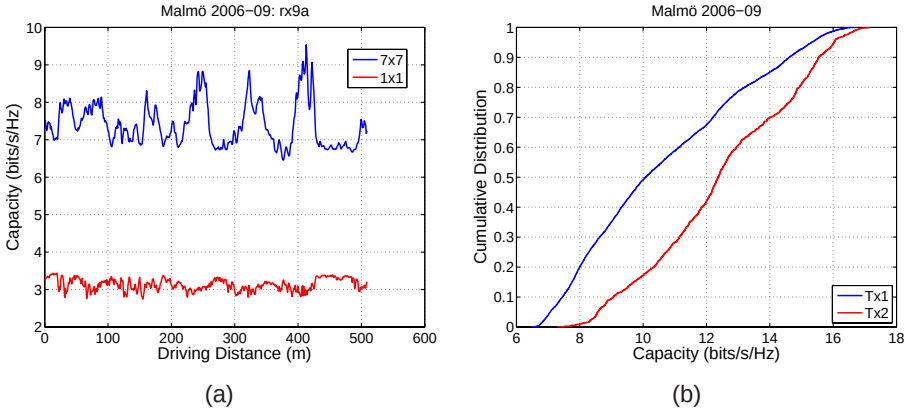


Figure 4.20: (a) Ergodic capacity vs. driving distance along Route 9 for Tx1. (b) CDF for the ergodic capacity measured from each Tx at an SNR of 10 dB.

have an SNR of at least the SNR level the capacity is evaluated for. Considering that the estimated noise level was estimated to correspond to a path gain of -138 dB, the measured path gain distribution in Figure 4.1(a) reveals that a number of measurements need to be excluded.

In Figure 4.20(a), the blue curve shows the $7 \times 7$ MIMO capacity at an SNR of 10 dB along Route 9 for Tx1. As a reference, the calculated SISO capacity between the (horizontally omnidirectional) center elements of the arrays is shown by the red curve. Again, we are going back to the measured path gain in Figure 4.3(a) for a comparison. We observe that the capacity variations along

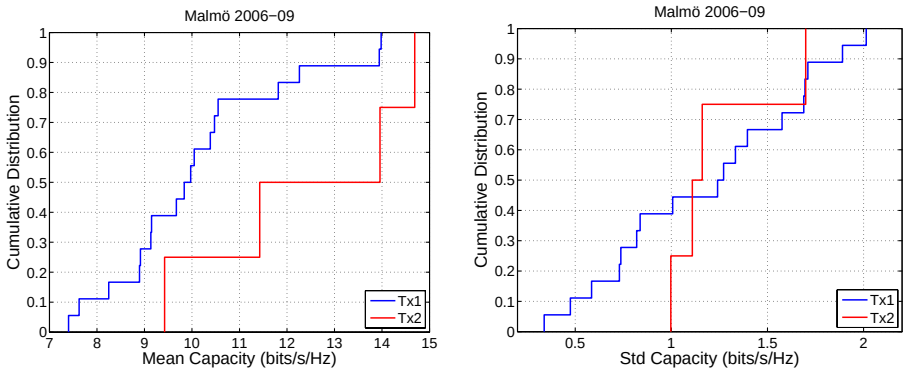


Figure 4.21: Ergodic capacity per-route statistics (SNR: 10 dB). (a) Mean value. (b) Standard deviation.

the route for the MIMO channel is to a large degree dependent on the measured path gain; where a higher path gain (higher received power) results in a lower capacity, and vice versa. This is since the results are evaluated at a fixed SNR.

The capacity distribution of all routes are shown in Figure 4.20(b) for a SNR of 10 dB. The capacity can be compared to the ergodic capacity for a $7 \times 7$ i.i.d. Rayleigh fading MIMO channel matrix, which for an SNR of 10 dB is 19.1 bits/s/Hz. The mean values of the measured ergodic capacities are about 52 % of a i.i.d. Rayleigh fading MIMO channel for Tx1 and 68 % for Tx2.

The per-route mean ($\overline{C}$) and standard deviation for the ergodic capacity at an SNR of 10 dB are shown in Figure 4.21. The variation in the per-route mean values is of the same order as for all routes together. The distribution for the zero-mean capacity variations $\widetilde{C} = C - \overline{C}$, at 10 dB SNR for the two Tx positions, is shown in Figure 4.22. By removing the per-route mean values, the spread in capacity has been significantly reduced. Hence, the capacity variations in the per-route environment is smaller than the global variations in the measured scenario.

## 4.7 Correlations

The correlation coefficients for a subset of estimated channel parameters and the channel capacity are shown in Table 4.1 for Tx1 and in Table 4.2 for Tx2. The capacity is here evaluated at a fix SNR of 10 dB. The exclusion of measurements with a lower measured SNR than 10 dB (see, Sec. 4.6) is equally applied for all parameters in this analysis.

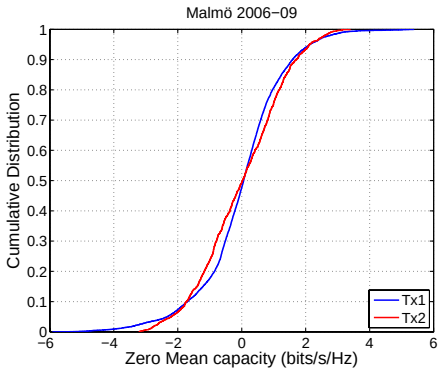


Figure 4.22: CDF for the ergodic capacity zero-mean process $\widetilde{C}$ (SNR: 10 dB).

| | $\log d$ | $G_{\text{meas}}$ | $G_{\text{LS}}$ | $K_{\text{dB}}$ | $\log \sigma_\tau$ | $C$ |
|---|---|---|---|---|---|---|
| $\log d$ | 1.00 | -0.82 | 0.02 | -0.14 | 0.50 | 0.12 |
| $G_{\text{meas}}$ | -0.82 | 1.00 | 0.55 | 0.55 | -0.80 | -0.59 |
| $G_{\text{LS}}$ | 0.02 | 0.55 | 1.00 | 0.75 | -0.67 | -0.87 |
| $K_{\text{dB}}$ | -0.14 | 0.55 | 0.75 | 1.00 | -0.59 | -0.74 |
| $\log \sigma_\tau$ | 0.50 | -0.80 | -0.67 | -0.59 | 1.00 | 0.71 |
| $C$ | 0.12 | -0.59 | -0.87 | -0.74 | 0.71 | 1.00 |

Table 4.1: Correlation coefficients for Tx1.

| | $\log d$ | $G_{\text{meas}}$ | $G_{\text{LS}}$ | $K_{\text{dB}}$ | $\log \sigma_\tau$ | $C$ |
|---|---|---|---|---|---|---|
| $\log d$ | 1.00 | -0.92 | 0.08 | -0.62 | 0.79 | 0.32 |
| $G_{\text{meas}}$ | -0.92 | 1.00 | 0.31 | 0.68 | -0.84 | -0.33 |
| $G_{\text{LS}}$ | 0.08 | 0.31 | 1.00 | 0.23 | -0.22 | -0.07 |
| $K_{\text{dB}}$ | -0.62 | 0.68 | 0.23 | 1.00 | -0.77 | -0.61 |
| $\log \sigma_\tau$ | 0.79 | -0.84 | -0.22 | -0.77 | 1.00 | 0.68 |
| $C$ | 0.32 | -0.33 | -0.07 | -0.61 | 0.68 | 1.00 |

Table 4.2: Correlation coefficients for Tx2.

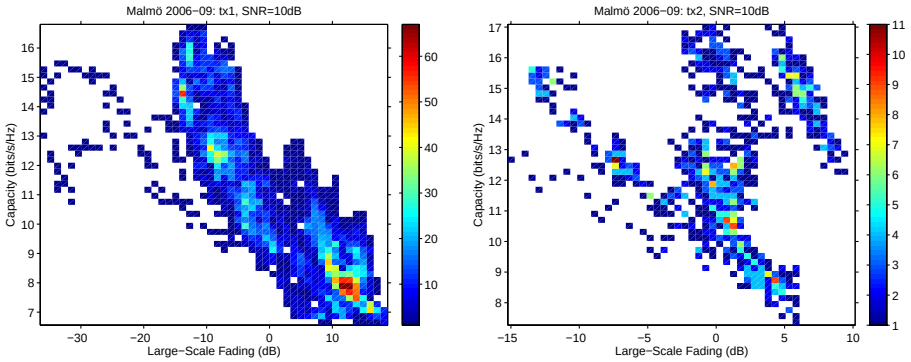


(a) Tx1: $C - G_{\mathrm{LS}}$ (b) Tx2: $C - G_{\mathrm{LS}}$

Figure 4.23: Joint distribution for Tx1 and Tx2 between ergodic capacity and large-scale fading.

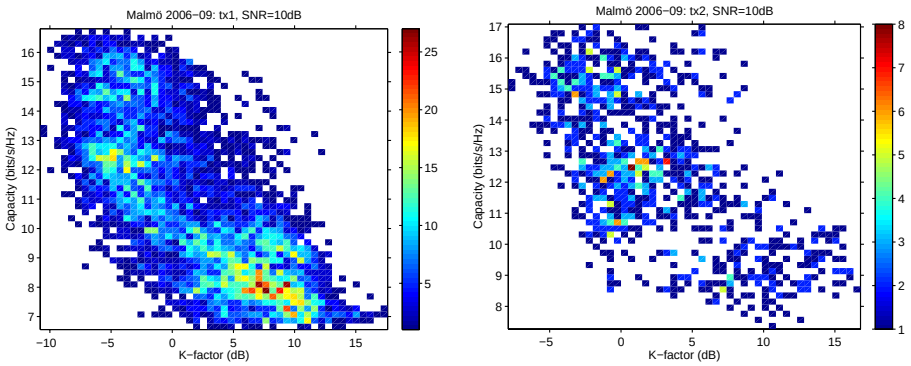


(a) Tx1: $C - K_{\mathrm{dB}}$ (b) Tx2: $C - K_{\mathrm{dB}}$

Figure 4.24: Joint distribution for Tx1 and Tx2 between ergodic capacity and $K$-factor.

For Tx1, the strongest correlations with the capacity are observed for the large-scale fading $G_{\mathrm{LS}}$ and the Ricean $K$-factor $K_{\mathrm{dB}}$ (both in dB), which is in line with the Linköping measurements, even though Tx1 is a elevated and the Linköping measurement is a peer-to-peer scenario. For Tx2, the same correlations can not be seen. The correlation with the large-scale fading is considerbly lower. On the other hand, for Tx2, the correlations are based on four measurement routes only and thus statistically less reliable results.

The correlation between capacity and large-scale fading for Tx1 is depicted

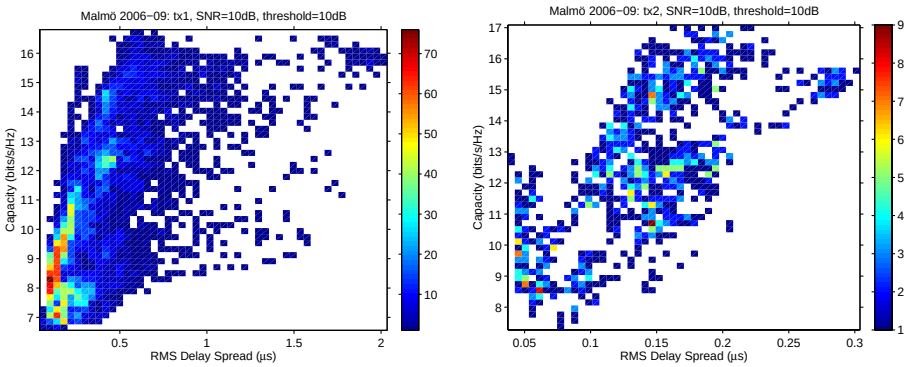


(a) Tx1: $C - \sigma_\tau$ (b) Tx2: $C - \sigma_\tau$

Figure 4.25: Joint distribution for Tx1 and Tx2 between ergodic capacity and RMS delay spread.

in Figure 4.23(a). The figure shows a 2-dimensional histogram where the color indicates the number in each bin. In the figure a major trend can be seen even if the result is scattered. The trend is that for low values of $G_{\mathrm{LS}}$ the capacity is high and for large values of the large-scale fading the capacity is low. Turning to the corresponding result for Tx2 in Figure 4.23(b), the same trend is not obvious. However, the Tx2 measurements are for only four routes and these can to some extent be distinguished in Figure 4.23(b). In fact, if the routes are considered separately, the same trend is seen. Thus, the four routes give a merged correlation with a small negative value, but separately, the routes give larger negative correlations.

Considering the correlation between capacity and large-scale fading for Tx1, a similar correlation between the $K$-factor and the capacity can be seen in Figure 4.24(a) for Tx1 and also in Figure 4.24(b) for Tx2. A low $K$ (indicating an amplitude distribution close to Rayleigh) results in high capacity, whereas a large $K$-factor (indicating a dominant LOS component) gives a low capacity.

The correlation coefficients between the capacity and the RMS delay spread indicate a clear correlation. A trend of higher capacity for higher delay spread is clear from Figure 4.25(a) and Figure 4.25(b), that is, both the elevated and the peer-to-peer scenario give the same trend.

# 5 Conclusions

The purpose of this work is to analyze the channel characteristics for urban environment at 300 MHz in order to derive information for a MIMO channel model usable for design and evaluation of future military MIMO systems.

In a previous report, the MIMO channel was measured along 25 Rx routes, with a total length of about 6 km, for 3 different Tx locations in the city of Linköping. Here, the channel was measured along 19 Rx routes for one of two Tx sites, named Tx1, and along 4 Rx routes for the other Tx site, named Tx2, in the city of Malmö. These routes cover both an elevated and a peer-to-peer scenarion. From the data, basic channel characteristics were extracted from the data as well as the ergodic capacity for the measured $7\times7$ MIMO channels at a fixed SNR. Two path-loss models was derived for the measured scenarios, i.e. the two Tx sites, and the distributions of the large-scale fading, the Ricean $K$-factor, the RMS delay spread, and the ergodic capacity were studied in detail. The correlation distance for the different channel parameters was also examined. In the following results are summarized:

- Two path-loss models are proposed, with path-loss exponents of about 4.56 for Tx1 and 4.41 for Tx2. The path-loss exponents are close to that for a flat-earth model, but the models have additional losses of about 17.68 for Tx1 and 14.37 dB for Tx2.

- The large-scale fading variations around the distance-dependent models are about $\pm15$ for the Tx1 and $\pm10$ dB for the Tx2 scenario, with standard deviations of about 9.48 dB for Tx1 and 4.99 dB for Tx2. It can be noted that the large-scale fading within the "local" per-route environments are significantly less than what is obtained for the global scenario. The median value of the per-route standard deviation is 3 dB, whereas the per-route mean values vary $\pm14$ dB. The mean value of the correlation distance of the large-scale fading is estimated to be about 41 m for Tx1 and 25 m for Tx2.

- The mean values of the Ricean $K$-factor are estimated to be about $0.92$ dB for Tx1 and $1.87$ dB for Tx2. The peer-route mean $K$-factors ranged from $-4$ to $8$ dB for Tx1 and from $-1$ to $8$ dB for Tx2. The correlation distance for the $K$-factor is, in general, very small, less than 5 m for 50% of the routes. It only exceeds 10 m for 26% of the routes.

- The mean values of the RMS delay spread are about 0.37 for Tx1 and 0.13 $\mu$s for Tx2. The per-route mean delay spread varies between $0.065$–

$1.5$ $\mu$s. The median correlation distance of the RMS delay spread is about 30 m.

- The mean values of the capacity are about 10 bits/Hz/s for Tx1 and 13 bits/s/Hz for Tx2 for a SNR of 10 dB. The median values of the measured ergodic capacity was about 52% for Tx1 and about 68% for Tx2 of the capacity for an i.i.d. Rayleigh fading MIMO channel. For Tx1, this is a bit less than for the mesurement campaign in Linköping. However, for the Tx1 scenario, the transmitter is located on a roof of a parking house, that is, this scenario is an elevated scenario rather than a peer-to-peer scenario resulting in less multipaths.

For most of the investigated parameters, the statistical analysis shows that the per-route distributions differ considerably compared to the corresponding global distribution for the scenarios. Furthermore, we show that many of the investigated parameters are correlated, e.g., the capacity is strongly correlated with the Ricean $K$-factor and with the large-scale fading, where the two latter parameters also are correlated. Moreover, the delay spread shows a strong correlation with the path loss.

# References


[1] R. Vaughan and J. B. Andersen, *Channels, Propagation and Antennas for Mobile Communications*. IEE Electromagnetic Waves Series, 2003.

[2] J. H. Winters, “On the capacity of radio communications systems with diversity in Rayleigh fading environments,” *IEEE J. Select. Areas Commun.*, vol. 5, pp. 871–878, Jun. 1987.

[3] G. J. Foschini and M. J. Gans, “On limits of wireless communications in a fading environment when using multiple antennas,” *Wireless Personal Commun.*, vol. 6, no. 3, pp. 311–335, 1998.

[4] I. E. Telatar, “Capacity of multi-antenna Gaussian channels,” *Eur. Trans. Telecommun.*, vol. 10, no. 6, pp. 585–595, Nov./Dec. 1999.

[5] A. F. Molisch and F. Tufvesson, “Multipath propagation models for broadband wireless systems,” in *Digital Signal Processing for Wireless Communications Handbook*, M. Ibnkahla, Ed. CRC Press, 2004, ch. 2, pp. 2.1–2.43.

[6] G. D. Durgin, V. Kukshya, and T. S. Rappaport, “Wideband measurements of angle and delay dispersion for outdoor and indoor peer-to-peer radio channels at 1920 MHz,” *IEEE Trans. Antennas and Propagat.*, vol. 51, no. 5, pp. 936–944, May 2003.

[7] D. Chizhik, J. Ling, D. Samardzija, and R. A. Valenzuela, “Spatial and polarization characterization of MIMO channels in rural environment,” in *Proc. 61st IEEE Veh. Technol. Conf. (VTC ’05 Spring)*, vol. 1, Stockholm, Sweden, May 2005, pp. 161–164.

[8] J. Ling, D. Chizhik, D. Samardzija, and R. A. Valenzuela, “Wideband and MIMO measurements in wooded and open areas,” in *Proc. IEEE AP-S Int. Symp.*, vol. 3B, Washington, USA, Jul. 2005, pp. 422–425.

[9] “ETSI EN 300 396-2: Trans-European Trunked Radio (TETRA); Technical Requirements for Direct Mode Operation (DMO); Part 2: Radio Aspects,” European Telecommunication Standards Institute, Tech. Rep., 2006.

[10] I. Z. Kovács, P. C. F. Eggers, K. Olesen, and L. G. Petersen, “Radio channel description and quality of service for TETRA direct mode operation in forest environments,” in *Proc. 54th IEEE Veh. Technol. Conf.*, Atlantic City, USA, Sep. 2001, pp. 1970–1974.

[11] J. R. Hampton, N. M. Merheb, W. L. Lain, D. E. Paunil, R. M. Shuford, and W. T. Kasch, “Urban propagation measurements for ground based communication in the military UHF band,” *IEEE Trans. Antennas and Propagat.*, vol. 54, no. 2, pp. 644–654, Feb. 2006.

[12] C. Hendrickson and C. Yerkes, “Wideband wireless peer to peer propagation measurements,” in *Thirty-Third Asilomar Conference on Signals, Systems, and Computers*, vol. 1, 1999, pp. 183–189.

[13] J. C. Liberti, J. C. Koshy, T. R. Hoerning, C. C. Martin, J. L. Dixon, A. A. Triolo, R. R. Murray, and T. G. McGiffen, “Experimental results using a MIMO test bed for wideband, high spectral efficiency tactical communications,” in *Proc. MILCOM 2005*, Oct. 2005.

[14] G. Eriksson, F. Tufvesson, and A. F. Molisch, “Propagation channel characteristics for peer-to-peer multiple antenna systems at 300 MHz,” in *Proc. IEEE GLOBECOM 2006*, San Francisco, USA, Nov. 2006.

[15] G. Eriksson, P. Holm, P. Johansson, S. Linder, and K. Wiklund, “Peer-to-peer MIMO channel measurements at 300 MHz in urban environment,” FOI, Linköping, Sweden, Report FOI-R--2547--SE, Jun. 2008.

[16] R. S. Thomä, D. Hampicke, A. Richter, G. Sommerkorn, and U. Trautwein, “MIMO vector channel sounder measurement for smart antenna system evaluation,” *European Transactions on Telecommunications*, vol. 12, no. 5, pp. 427–438, Sep. / Oct. 2001.

[17] RUSK channel sounder — Measurement principle. [Online]. Available: http://www.channelsounder.de/ruskchannelsounder.html

[18] C. Tepedelenlioğlu, A. Abdi, and G. B. Giannakis, “The Ricean $K$ factor: Estimation and performance analysis,” *IEEE Trans. Wireless. Commun.*, vol. 2, no. 4, pp. 799–810, Jul. 2003.

[19] Y. Chen and N. C. Beaulieu, “Maximum likelihood estimation of the $K$-factor in Ricean fading channels,” *IEEE Communications Letters*, vol. 9, no. 12, pp. 1040–1042, Dec. 2005.

[20] K. E. Baddour and T. J. Willink, “Improved estimation of the Ricean K factor from I/Q samples,” in *Proc. 66th IEEE Veh. Technol. Conf. (VTC 2007 Fall)*, Baltimore, MA, USA, Sep./Oct. 2007, pp. 1228–1232.

[21] S. Wyne, A. F. Molisch, P. Almers, G. Eriksson, J. Karedal, and F. Tufvesson, “Outdoor-to-indoor office MIMO measurements and analysis at 5.2 GHz,” *IEEE Trans. Veh. Technol.*, vol. 57, no. 3, pp. 1374–1386, May 2008.

[22] M. Steinbauer, A. F. Molisch, and E. Bonek, “The double-directional radio channel,” *IEEE Antennas Propag. Mag.*, vol. 43, no. 4, pp. 51–63, 2001.

[23] A. F. Molisch, *Wireless Communications*. IEEE Press – Wiley, 2005.

[24] V. Erceg, L. J. Greenstein, S. Y. Tjandra, S. R. Parkoff, A. Gupta, B. Kulic, A. A. Julius, and R. Bianchi, “An empirically based path loss model for wireless channels in suburban environments,” *IEEE J. Select. Areas Commun.*, vol. 17, no. 7, pp. 1205–1211, Jul. 1999.

[25] H. Asplund, A. A. Glazunov, A. F. Molisch, K. I. Pedersen, and M. Steinbauer, “The COST 259 directional channel model–Part II: Macrocells,” *IEEE Trans. Wireless. Commun.*, vol. 5, no. 12, pp. 3434–3450, Dec. 2006.

[26] C. Oestges and B. Clerckx, “Modeling outdoor macrocellular clusters based on 1.9-GHz experimental data,” *IEEE Trans. Veh. Technol.*, vol. 56, no. 5, pp. 2821–2830, Sep. 2007.